JGR Space Physics

RESEARCH ARTICLE
10.1029/2023JA032274

Evening Solar Terminator Waves in Earth's Thermosphere: Neutral Wind Signatures Observed by ICON-MIGHTI

L. Claire Gasque[1], Brian J. Harding[1], Thomas J. Immel[1], Yen-Jung Wu[1], Colin C. Triplett[1], Sharon L. Vadas[2], Erich Becker[2], and Astrid Maute[3]

[1]Space Sciences Laboratory, University of California, Berkeley, Berkeley, CA, USA, [2]Northwest Research Associates, Boulder, CO, USA, [3]Cooperative Institute for Research in Environmental Sciences, University of Colorado, Boulder, Boulder, CO, USA

Key Points:

- Thermospheric wind measurements above 200 km show a prominent migrating wave associated with the evening solar terminator
- The first observations of solar terminator wave altitude profiles reveal >200 km vertical wavelengths above 200 km
- Comparison with numerical models suggests a lower atmospheric origin and the potentially significant role of gravity waves

Supporting Information:

Supporting Information may be found in the online version of this article.

Correspondence to:

L. C. Gasque,
lcgasque@berkeley.edu

Citation:

Gasque, L. C., Harding, B. J., Immel, T. J., Wu, Y.-J., Triplett, C. C., Vadas, S. L., et al. (2024). Evening solar terminator waves in Earth's thermosphere: Neutral wind signatures observed by ICON-MIGHTI. *Journal of Geophysical Research: Space Physics*, *129*, e2023JA032274. https://doi.org/10.1029/2023JA032274

Received 10 NOV 2023
Accepted 29 JAN 2024

Abstract The moving solar terminator (ST) generates atmospheric disturbances, broadly termed solar terminator waves (STWs). Despite theoretically recurring daily, STWs remain poorly understood, partially due to measurement challenges near the ST. Analyzing Michelson Interferometer for Global High-resolution Thermospheric Imaging (MIGHTI) data from NASA's Ionospheric Connection Explorer (ICON) observatory, we present observations of STW signatures in thermospheric neutral winds, including the first reported meridional wind signatures. Seasonal analysis reveals STWs are most prominent during solstices, when they intersect the ST about ∼20° latitude from the equator in the winter hemisphere and have phase fronts inclined at a ∼40° angle to the ST. We also provide the first observed STW altitude profiles, revealing large vertical wavelengths above 200 km. Comparing these observations to four different models suggests the STWs likely originate directly or indirectly from waves from below 97 km. STWs may play an under-recognized role in the daily variability of the thermosphere-ionosphere system, warranting further study.

Plain Language Summary Every evening, the sunset removes the primary energy input to the upper atmosphere, causing rapid atmospheric cooling and generating disturbances called solar terminator waves (STWs). Although they theoretically occur every night, STWs remain poorly understood, partially because the rapidly changing atmospheric conditions near sunset make measurements challenging. This study examines neutral wind measurements from the Michelson Interferometer for Global High-resolution Thermospheric Imaging (MIGHTI) on board NASA's Ionospheric Connection Explorer (ICON) observatory to uncover signatures of STWs. We report the north-south wind signatures of STWs and their altitude profile from 200 to 300 km, both of which have never been previously reported. We show that STWs are some of the largest amplitude dynamical features above 200 km near solstices, but are much weaker near equinoxes. By comparing our observations with the outputs of four different models, we find that STWs are likely generated directly or indirectly (from wave propagation) below 97 km. Future work is necessary to better understand how STWs are generated, how they vary on a daily basis, and the extent of their impacts on Earth's upper atmosphere.

1. Introduction: Solar Terminator Waves in the Terrestrial Thermosphere

Every night, the evening solar terminator (ST) sweeps across Earth, dividing daylight from shadow and interrupting the solar radiation which plays a key role in atmospheric heating and ionospheric plasma production. This generates abrupt gradients in atmospheric temperature and pressure, which can launch disturbances in the mesosphere and thermosphere (Somsikov, 2011). Broadly termed solar terminator waves (STWs), these disturbances form near and propagate with the advancing ST (Miyoshi et al., 2009). Although they theoretically recur every night, STWs' morphology and occurrence patterns remain poorly characterized, and their specific generation mechanisms are still debated.

STW generation theory first emerged when, inspired by Chimonas and Hines (1970)'s anticipation of gravity waves excited by time-variable heating during solar eclipses, Beer (1973) proposed a similar effect from the daily motion of the ST. Subsequent research delved deeper into the theoretical underpinnings of STWs, generally confirming that the moving ST can generate gravity waves, but the scarcity of observations hampered further advancement of this work (Beer, 1978; Cot & Teitelbaum, 1980; Somsikov, 1987; Somsikov & Ganguly, 1995).

Only three studies have reported observations of STWs in the thermosphere. Using the CHAMP satellite's triaxial accelerometer, Forbes et al. (2008) identified an STW in thermospheric neutral densities. These had a

~3,000 km horizontal wavelength, had phase fronts inclined ~30° with respect to the ST, and were more pronounced during solstices than equinoxes. Subsequently, H. Liu et al. (2009) confirmed the density STW and also detected an STW in CHAMP's thermospheric cross-track (i.e., mainly zonal) winds. The zonal wind STW had comparable wavelength and inclination to the ST as the density STW, with zonal wind magnitudes ranging from 5 to 15 m/s, constituting 5%–20% of the mean zonal wind velocity at those local times. Both studies concluded that the STW was more prominent at dusk than at dawn, with most wave structures appearing on the nightside, only extending into the sunlit region around solstices. These results correlated well with General Circulation Model (GCM) simulations conducted by Forbes et al. (2008) and Miyoshi et al. (2009). In a third study, Bespalova et al. (2016) examined in-situ neutral density perturbations detected by the Atmospheric Explorer-E satellite, finding density perturbations with amplitudes of 2%–4% associated with the ST passage.

Recent modeling by Chou et al. (2022) and Vadas et al. (2023) suggests that STWs in neutral winds could have a more significant impact on equatorial thermospheric dynamics than previously considered. Using a Specified Dynamics Whole Atmosphere Community Climate Model with thermosphere-ionosphere eXtension (SD-WACCM-X) simulation from October 2020, Chou et al. (2022) identified a large-amplitude evening STW with phase fronts aligned from northwest to southeast, the same orientation as winter solstice STWs observed with CHAMP (Forbes et al., 2008; H. Liu et al., 2009). Chou et al. (2022) proposed that evening STWs play an underrecognized role in driving equatorial electrodynamic phenomena such as equatorial plasma bubbles (EPBs). Additionally, Vadas et al. (2023) identified STWs with horizontal wind magnitudes of 50–100 m/s in a HIgh Altitude Mechanistic general Circulation Model (HIAMCM) simulation of 15 January 2022. Although their primary focus was simulating the primary and secondary gravity waves triggered by the Hunga Tonga-Hunga Ha'apai volcanic eruption, the STW was surprisingly prominent in the simulation results and interacted nonlinearly with the eruption-induced gravity waves. While both studies report STWs with significant neutral wind amplitudes and emphasize their potential influence on thermospheric and ionospheric dynamics, these conclusions remain to be confirmed with observational evidence.

This study presents the first remotely sensed measurements of evening STWs in thermospheric neutral winds, including the first STW meridional wind observations. By analyzing ~1.5 years of data from NASA's Ionospheric Connection Explorer (ICON) satellite, we investigate seasonal variation in STWs, and compare these findings to simulations from several models. We also present the first observed altitude profiles of thermospheric evening STWs, comparing our observations with HIAMCM simulation results. This work confirms that STWs are prominent features in the terrestrial thermosphere, suggesting the necessity of future modeling and observational studies which will further enhance our understanding of STW drivers and effects.

2. Methods: Observations and Modeling

2.1. ICON/MIGHTI Neutral Wind Observations

In this study, we examine evening STW signatures in neutral wind measurements from ICON's Michelson Interferometer for Global High-Resolution Thermospheric Imaging (MIGHTI). ICON follows a nearly circular orbit with 27° inclination at ~600 km and achieves complete local time coverage across sampled latitudes every ~48 days (Immel et al., 2018). Further details about ICON's design and objectives can be found in Immel et al. (2018), and the significant findings from its prime mission period are outlined in Immel et al. (2023).

MIGHTI measures Doppler shifts in oxygen red-line (630.0 nm) and green-line (557.7 nm) airglow emissions to determine horizontal neutral wind profiles between −12° and +42° latitude (Englert et al., 2017). Unlike CHAMP, which made in situ measurements, ICON remotely measures neutral wind altitudinal profiles, enabling observations of the vertical structure of STWs. MIGHTI captures daytime wind profiles every 30 s between 90 and 300 km. Nighttime winds are sampled every 60 s at the same altitudes, except for a gap spanning ~109–210 km where the airglow brightness is insufficient to take reliable measurements (Harding et al., 2021; Harlander et al., 2017).

Here, we use MIGHTI Level 2.2 Version 5 data, which provides meridional and zonal neutral wind measurements (Harding et al., 2023a, 2023b). Near the ST, there is a brief (typically <5 min) data gap when MIGHTI switches from day to night mode (Englert et al., 2023). Additionally, the MIGHTI wind retrieval algorithm assumes that the atmosphere is spherically symmetric, but this assumption is violated by the rapidly changing conditions near the ST (Harding et al., 2017). While the resulting asymmetry-associated errors can surpass 10 m/s near 150 km, above

200 km these errors are expected to be less than 1 m/s and therefore should not affect our analysis (Wu et al., 2020). Furthermore, Version 5 incorporates three updates important for improving the wind data quality near the ST: an independent, higher accuracy zero-wind calibration, an updated thermal drift correction, and a correction for the "anomalous low-signal phase shift" (Englert et al., 2023). Additional details about the MIGHTI instrument design and data processing can be found in Englert et al. (2017), Harding et al. (2017), and Harlander et al. (2017), while the updated Version 5 processing is detailed in Englert et al. (2023).

Due to the significant variations in STW morphology between seasons (Forbes et al., 2008; H. Liu et al., 2009), we divide the data into three seasons for analysis: northern hemisphere (NH) winter, combined equinox, and NH summer. Spring and autumn are combined as they exhibit minimal differences in our analysis. For each season, we include data captured in the period from 45 days before to 45 days after the corresponding solstice or equinox, encompassing 90 days total or nearly 2 full precession cycles. While MIGHTI data is available almost continuously from December 2019 to November 2022, the SD-WACCM-X simulations used for comparison (see Section 2.2) only extend until 27 March 2021. Consequently, we limit our analysis to this period (December 2019–March 2021), covering 2 NH winters, nearly 3 equinoxes, and 1 NH summer. Extending our analysis to the end of the mission does not alter our observational conclusions (refer to the Supporting Information S1 for the results for the full ICON mission). With the exception of some moderate solar activity in November 2020, all of the data surveyed here is for solar quiet ($F10.7 < 80$) conditions (Wu et al., 2023). This period also encompasses a small geomagnetic storm, described in McGinness et al. (2023).

We bin the meridional and zonal winds for each season into 30-min solar local time (SLT) intervals and 1° latitude bins, taking the median value in each bin. We take the median to minimize the influence of outliers arising from artifacts near the terminator. By averaging over all longitudes, we selectively retain features traveling with Earth's rotation, filtering out non-migrating components (Miyoshi et al., 2009). MIGHTI's horizontal resolution is affected by its integration time, horizontal field of view, line-of-sight averaging, and the spacecraft velocity, as detailed in Harding et al. (2021)'s Appendix. We reproduced (Harding et al., 2021)'s analysis for the MIGHTI red-line measurements, finding that near 280 km, where we report STW amplitudes and scale sizes in this work, these combined effects generate a horizontal averaging kernel of ∼700 km. Our 30-min SLT bins are equivalent to roughly 850 km resolution. Given an expected evening STW scale size of ∼3,000 km (Forbes et al., 2008), the resolution is sufficient for capturing these features. Although data sampled within ∼500 km of the ST carries a "caution" label in MIGHTI's data quality flags, we nonetheless include this data in our analysis. Despite binning and averaging the data, some artifacts near the ST persist, especially in NH summer where we incorporate only a single season of data. However, since any data artifacts have a much smaller scale than the evening STWs, and are oriented exactly parallel to the ST, they are not expected to affect our conclusions.

In the cases where we find the largest evening STW amplitudes, we further characterize the STW's morphology. First, we remove diurnal variations as a function of SLT at each latitude by fitting and subtracting a 24-hr period sinusoid (representing the diurnal tide). Then, we perform a least-squares fit of a Gaussian near the evening ST at each latitude, determining the amplitude and defining the scale size as the full-width at half-maximum (FWHM). The reported amplitudes and scale sizes in Section 3 represent averages across all latitudes observed by MIGHTI. By fitting a line to the STW as a function of latitude and SLT and intersecting it with the ST's position, computed using the method described in Colonna and Tramutoli (2021), we determine the latitude of intersection and the STW's angle relative to the ST.

2.2. Simulations

To determine whether current global models capture the physics necessary to reproduce STW signatures observed by MIGHTI, we compare the observations to simulations from three different models: the Thermosphere-Ionosphere-Electrodynamics General Circulation Model for the Ionospheric Connection Explorer (TIEGCM-ICON) (Maute, 2017), SD-WACCM-X 2.0 (H.-L. Liu et al., 2018; Maute & HAO WACCM team, 2022), and the HIAMCM (Becker, Goncharenko, et al., 2022; Becker, Vadas, et al., 2022; Becker & Vadas, 2020, 2022).

The TIEGCM describes thermospheric and ionospheric dynamics, energetics, and chemistry, coupled with ionospheric electrodynamics (Qian et al., 2014; Richmond, 1995). In this study, we used TIEGCM-ICON, ICON's Level 4 data product (Maute, 2017; Maute et al., 2023; Maute & ICON Team, 2022), which includes two runs of the TIEGCM: a simulation which incorporates data-driven 42-day averages of diurnal and semidiurnal tidal forcing at the 97 km lower boundary via the Hough Mode Extension (HME) from MIGHTI horizontal winds

and temperatures (Cullens et al., 2020; Forbes et al., 2017), and one without such a tidal specification. The background at the lower boundary is obtained from global averages of horizontal winds (Drob et al., 2008) and neutral temperatures and densities (Picone et al., 2002). The model resolution is 2.5° by 2.5° in geographic latitude and longitude and the numerical damping suppresses features with wavelengths below ∼2,500 km. This model does not include gravity waves generated below its lower boundary, although it implicitly incorporates some effects of turbulent mixing due to gravity wave breaking by specifying the eddy diffusivity at the lower boundary (Qian et al., 2014). This method does not, however, account for the spatial distribution of lower/middle atmosphere gravity wave sources.

Unlike the TIEGCM, SD-WACCM-X 2.0 includes lower atmospheric dynamics to capture large-scale day-to-day variations (H.-L. Liu et al., 2018). We use the run performed by England et al. (2022), which is nudged to GEOS-5 (Maute & HAO WACCM team, 2022). The detailed lower atmospheric physics, including tropospheric weather, deep convection, and ozone variability, are described by Marsh et al. (2013) and Neale et al. (2013). The SD-WACCM-X simulations we use have 0.9° by 1.25° resolution in latitude and longitude, respectively, capable of resolving features with wavelengths larger than ∼500 km. To account for small-scale gravity wave momentum deposition, SD-WACCM-X includes a gravity wave parametrization, detailed by Richter et al. (2010) and Garcia et al. (2017), which identifies gravity wave sources (e.g., convection, fronts, orographic features) and incorporates resulting wave dissipation effects into the simulations.

The TIEGCM (with and without HMEs) and SD-WACCM-X simulations in this analysis cover the period from ICON mission's start until spring 2021. We sampled model outputs at the same times and locations as MIGHTI data, and processed this "synthetic data" in the same manner as the MIGHTI data (described in Section 2.1).

We also compare NH winter STW results from the HIAMCM, a high-resolution global whole-atmosphere model for neutral dynamics. The HIAMCM's horizontal grid spacing is ∼52 km (∼0.45°), enabling it to effectively resolve waves with horizontal scales above ∼200 km, smaller than the TIEGCM and SD-WACCM-X simulations examined here (Becker, Vadas, et al., 2022). This model also incorporates lower atmospheric processes, detailed in Becker and Vadas (2020), with large scales nudged to Modern-Era Retrospective analysis for Research and Applications, Version 2 (MERRA-2) reanalysis up to ∼70 km. Unlike the other models, the HIAMCM explicitly resolves gravity waves, including both primary gravity waves and the secondary gravity waves which arise from dissipation of the primaries (Becker, Goncharenko, et al., 2022; Becker & Vadas, 2020). Resolved gravity wave packets that become dynamically unstable are damped by physics-based subgrid-scale turbulent diffusion, simulating wave-mean flow interactions caused by wave instability and subsequent dissipation (Lindzen, 1981). The HIAMCM neglects non-local momentum and energy transfer caused by non-resolved gravity waves.

This study uses the HIAMCM "background" run from 15 January 2022, which excludes the effects of the Tonga volcano eruption on that day and the geomagnetic storm on the day prior (Becker & Vadas, 2022; Vadas et al., 2023). To facilitate comparisons, we bin and average the data from every time step of the simulation as functions of the same latitude and SLT bins used for MIGHTI and extract the STW features in the same manner.

3. Results

Figure 1a presents NH winter MIGHTI meridional winds at ∼283 km, binned and averaged as a function of latitude and SLT. This altitude was chosen to minimize terminator-related data artifacts. Gray shading marks nighttime regions (for which the sun is below the horizon) at this altitude. Note that, although none of the tides have been removed in Figure 1a, the evening STW is a prominent feature in the meridional winds, appearing as a northward wind enhancement near the evening ST (the transition between illumination and shadow near 20 SLT). At most MIGHTI-sampled latitudes, the STW-related enhancement corresponds to the largest total meridional wind amplitude with respect to SLT, suggesting its potentially significant role in thermospheric and ionospheric dynamics, including field-aligned ion drag and interhemispheric transport (Heelis et al., 2022).

The second row of Figure 1 shows the tidal decomposition of Figure 1a into its diurnal (Figure 1b), semidiurnal (Figure 1c), and terdiurnal (Figure 1d) components. These components were obtained by fitting sinusoids with 24-hr, 12-hr, and 8-hr periods, respectively, as a function of SLT at each latitude. The amplitude of the colorbar is reduced for each successive tidal component, reflecting the diminishing power in each subsequent component. The final row (Figures 1e–1g) displays the residuals in the data after removing each successive tidal component.

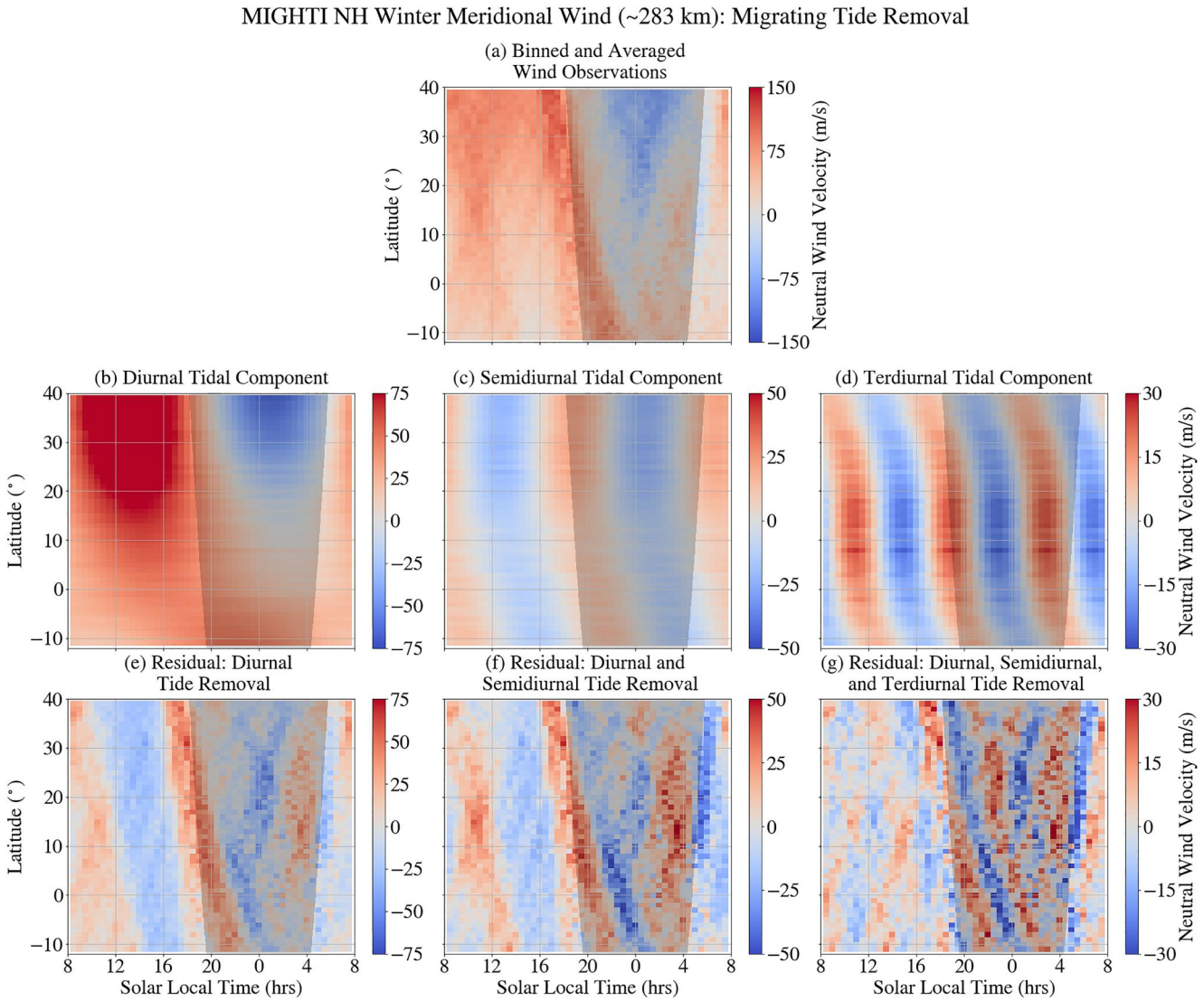

Figure 1. Meridional winds during NH winter as observed by MIGHTI, presented as a function of latitude and SLT. In the first row, (a) shows the binned and averaged data prior to the removal of tidal components. The second row displays the fits for the (b) diurnal, (c) semidiurnal, and (d) terdiurnal tidal components. The final row shows the data residuals after successively removing the (e) diurnal, (f) semidiurnal, and (g) terdiurnal tides. Note that the colorbar amplitude varies between subfigures.

Figure 2 shows the corresponding tidal decomposition of the observed zonal winds. In this case, the diurnal tide is more dominant than in the meridional winds, with the binned wind measurements in Figure 2a showing a clear pattern of westward winds during the day and eastward winds at night. However, with the removal of the diurnal tidal component (Figure 2e), an enhanced eastward wind feature emerges which has a similar amplitude and proximity to the evening ST as the northward meridional wind enhancement.

With the successive removal of the migrating diurnal, semidiurnal, and terdiurnal tidal components, the STW amplitude is reduced, although a distinct signature persists. This suggests the STW has power in multiple tidal components and is not attributable to any individual tide. Therefore, in the subsequent analysis, we characterize the STW after removing only the migrating diurnal tidal component.

Figure 3 displays binned MIGHTI meridional and zonal winds at ~283 km for NH winter, combined equinox, and NH summer after removing the migrating diurnal tide. Black dotted lines identify the STW feature in the solstice cases. The NH winter STW is characterized by ~50 m/s northward winds (Figure 3a) and ~50 m/s eastward winds on the nightside, although the zonal wind component diminishes on the dayside (Figure 3b). In both meridional and zonal wind components, it has a ~3,400 km scale size (calculated as described in Section 2.1),

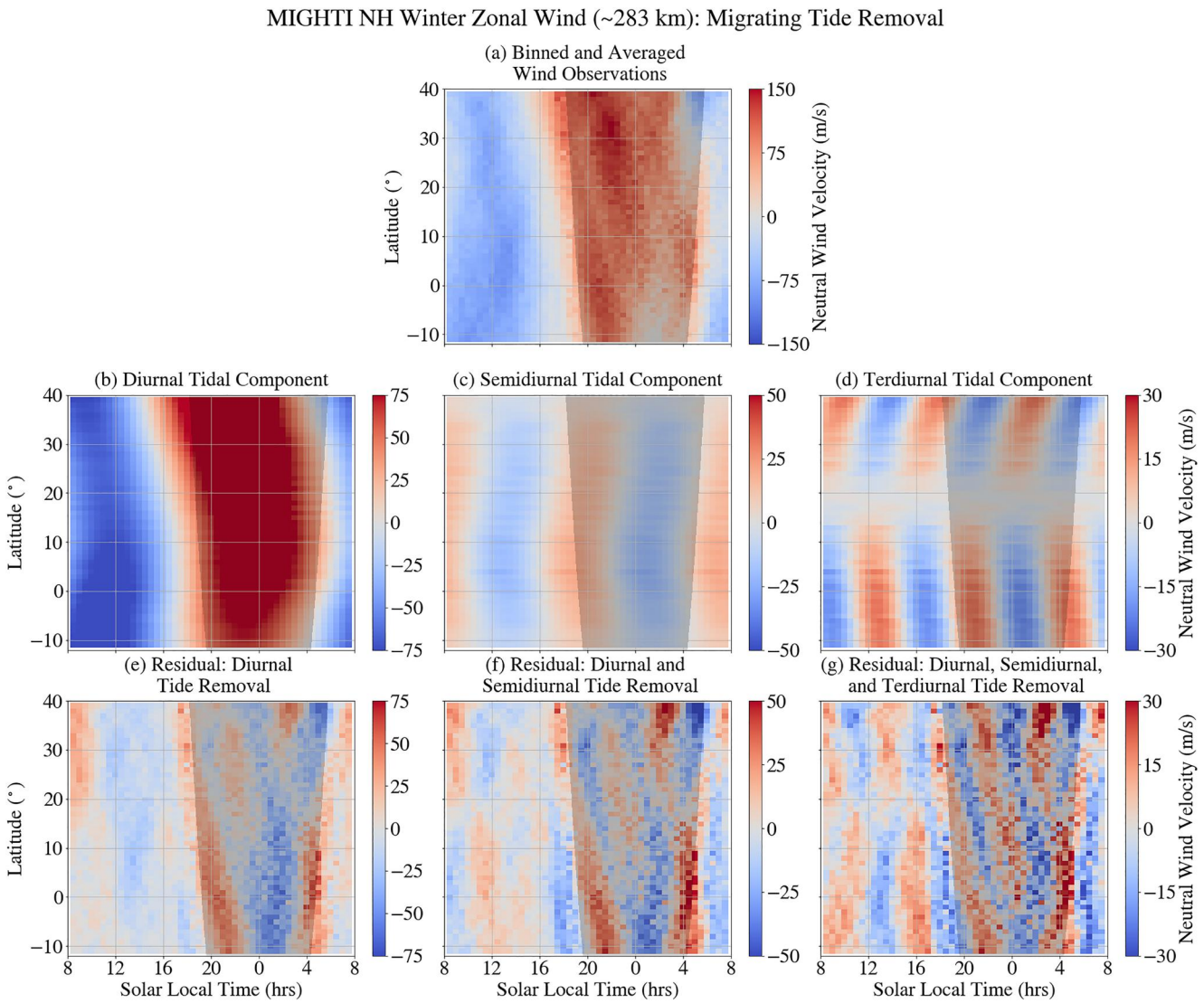

Figure 2. Same as Figure 1, but for the observed zonal wind component.

intersecting the ST between ~15°–20° latitude (~18.8 SLT) with a ~31° phase front inclination compared to the ST.

For the NH summer case, MIGHTI's latitude sampling does not reach father south than −12°, where we might expect the NH summer STW to intersect the evening ST. However, we observe a ~40 m/s southward wind enhancement (Figure 3e) and a ~25 m/s eastward wind enhancement (Figure 3f), whose phase fronts, when extrapolated down to lower latitudes, intersect the evening ST between ~−20° to −25° latitude (~18.6 SLT). The scale size of this feature is ~2,700 km, comparable to the NH winter STW, and its phase front is inclined ~41° relative to the ST at the intersection point. Although there is also a strong northward wind component close to the evening ST and therefore associated with the evening STW during NH summer, a data artifact near the ST prevents us from characterizing it fully.

In combined equinox, the STW is less evident, even after removing diurnal tides (Figures 3c and 3d), consistent with Forbes et al. (2008)'s findings of seasonal asymmetry.

The NH winter and NH summer STWs mirror each other. The NH winter STW wavefront stretches from northwest to southeast with winds blowing northeast, while the NH summer STW wavefront extends from northeast to southwest with winds blowing southeast. Both have phase fronts inclined relative to the ST and

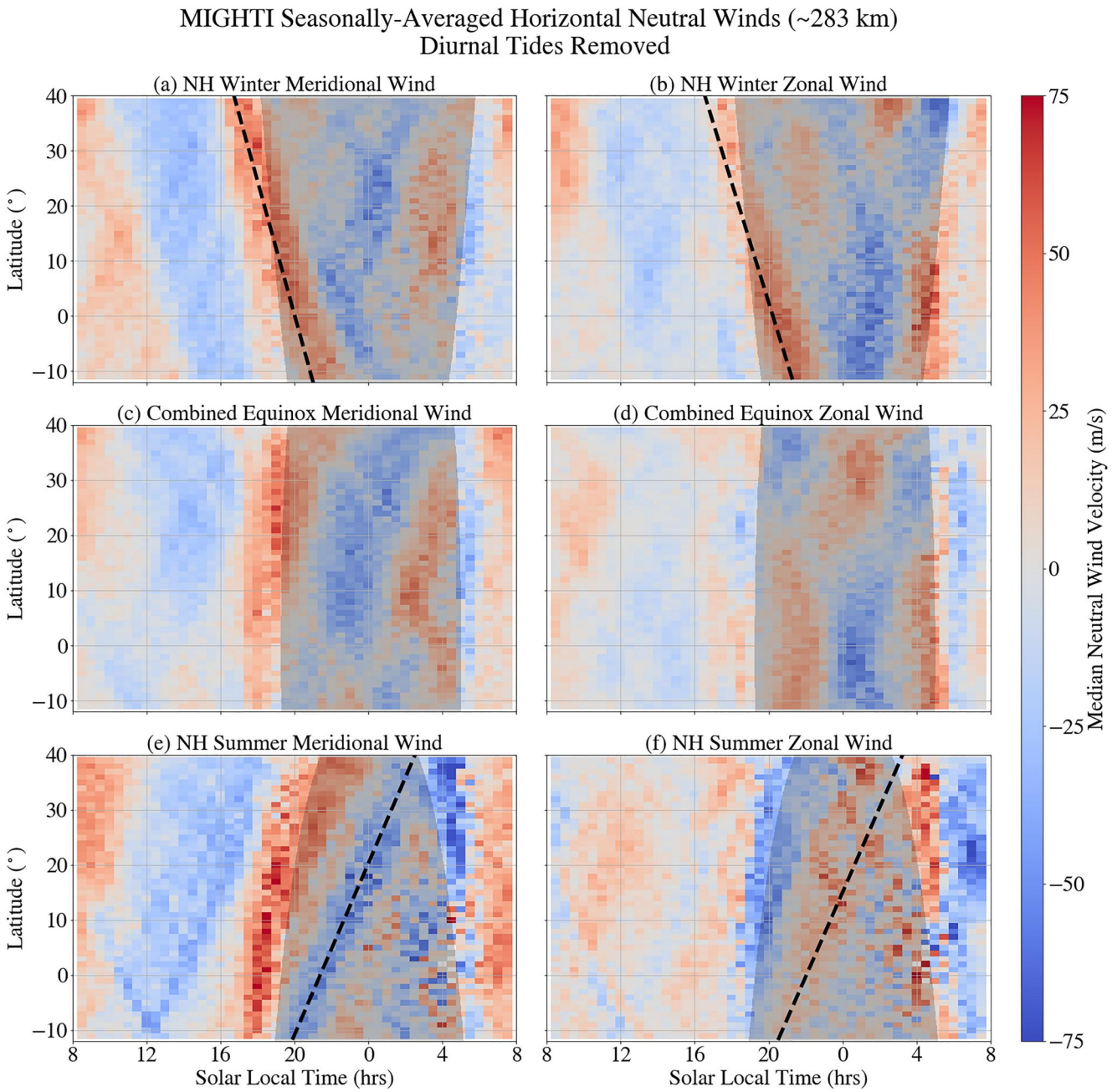

Figure 3. Binned and averaged MIGHTI meridional (left column) and zonal (right column) neutral winds for NH winter (top row), combined equinox (middle row), and NH summer (bottom row). Diurnal tides have been removed. Northward and eastward winds are positive. The gray shading shows the portion of the latitude/SLT space that is in darkness for each season. Clear STW features are marked by a black dotted line for the solstice cases (a, b, e, f).

intersect it ~20° off the equator in the winter hemisphere, near 18.7 SLT. The persistent presence of the STW in solstice winds, even with long-term averaging, shows that it is a robust feature. While there is likely day-to-day variability, the large average magnitude of the STW implies that it is a dominant feature in thermospheric winds, at least under solstice solar quiet conditions.

While it is tempting to quantitatively compare our estimated amplitudes to previous studies, each study used a different filtering method, so it is necessary to use caution. Miyoshi et al. (2009) removed diurnal, semidiurnal, and terdiurnal tidal components from their simulation results, Forbes et al. (2008) applied high-pass filtering with a 4,800 km wavelength cutoff to CHAMP neutral density data, and H. Liu et al. (2009) subtracted a third order

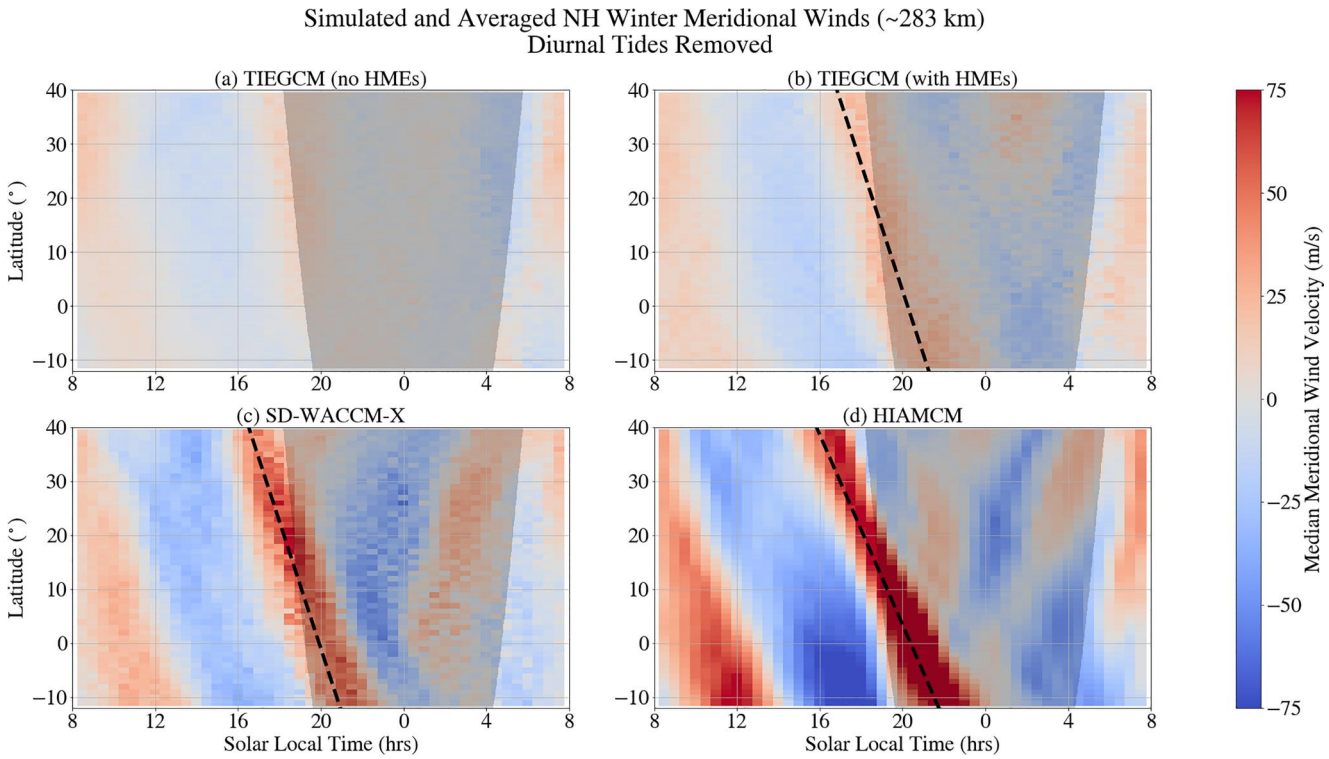

Figure 4. Each panel shows NH winter meridional winds binned by latitude and SLT with diurnal tides removed (the same as Figure 3a), but for (a) TIEGCM simulations without HME inputs, (b) TIEGCM simulations with HMEs derived from MIGHTI observations, (c) SD-WACCM-X simulations, and (d) HIAMCM simulations. The first three simulation results incorporate winter 2019 and 2020, while the HIAMCM result is from 15 January 2022.

polynomial from CHAMP densities and zonal winds along each satellite track. This makes an analogous ICON analysis impossible due to the difference in orbital inclinations. Both Vadas et al. (2023) and Chou et al. (2022) presented unfiltered simulation results. The figures we show are binned and averaged to remove the non-migrating tidal features, and we report STW amplitudes after having removed the diurnal tide.

Analyzing simulation outputs alongside MIGHTI observations provides insight into the origins of STWs. Figure 4 displays NH winter meridional winds simulated by four different models, all with diurnal tides removed. In the TIEGCM run without HMEs (Figure 4a), there is no clear STW signature, though a weak (~25 m/s) signature appears when HMEs are included (Figure 4b). In contrast, both SD-WACCM-X (Figure 4c) and HIAMCM simulations (Figure 4d) exhibit a distinct STW signature. Both models overestimate the STW amplitude relative to observations, with SD-WACCM-X producing ~60 m/s northward winds and HIAMCM producing ~100 m/s northward winds. It is important to be cautious when interpreting the HIAMCM's STW amplitude, however, as it is based on a single day and is not averaged like the other models and observations. It is possible that the amplitude is high in this case simply because the STW was particularly strong on this day and that an average, considering more daily variability, would reduce the amplitude. The slight amplitude overestimation in SD-WACCM-X is real since the SD-WACCM-X simulations are sampled identically to MIGHTI. Both models generally capture the STW's scale size and phase front inclination with respect to the ST.

The same figure, but showing the modeled zonal winds, is presented in Figure 5. Again, the TIEGCM run without HMEs (Figure 5a) shows little evidence of an evening STW. The case with HMEs does show an eastward wind enhancement near the evening ST, but the phase front is not comparably inclined with respect to the ST as the observed STW and does not intersect the ST at the sampled latitudes. Therefore, even with HMEs driving the lower boundary, the TIEGCM does not appear to accurately reproduce the observed evening STW. Both the SD-WACCM-X and HIAMCM simulations capture the STW signature in the zonal winds, although the signal does not diminish on the dayside as much as it does in the observations. Further discussion on the implications of STW appearance or absence in the various models is found in Section 4.

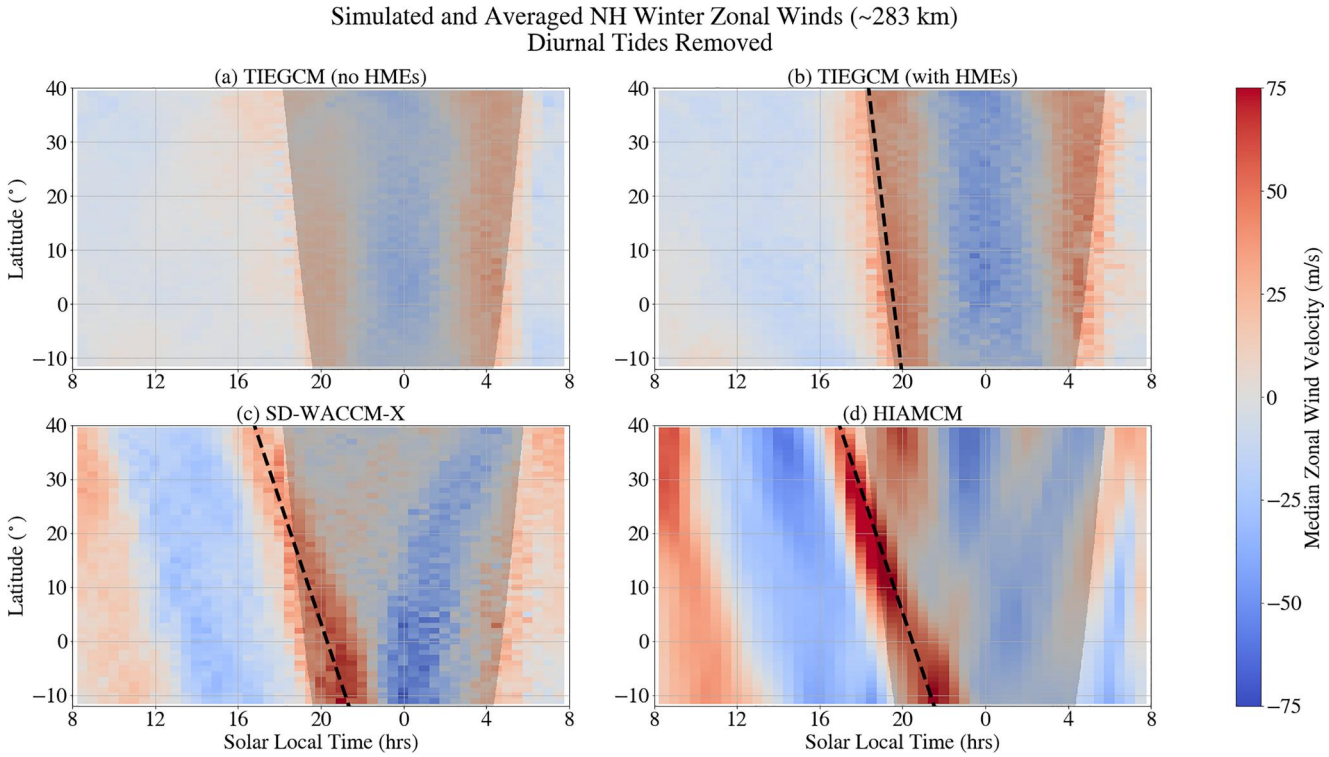

Figure 5. Same as Figure 4, but for the modeled zonal wind component.

Figures 6a and 6b display the altitude structure of the NH winter STW in MIGHTI meridional winds and zonal winds, respectively. The data have been averaged data between 10° and 20° latitude, where the STW intersects the ST, and diurnal tides have been removed. Although MIGHTI data is available between 109 and 200 km during the day, the nighttime gap precluded the removal of diurnal tides at these altitudes, so we do not report any data in this altitude range.

Above 200 km, where nighttime MIGHTI data is available, the STW has a vertical wavelength greater than 200 km. Below 115 km, the STW is not distinguishable, although it may be masked by the large-amplitude tides at these altitudes. The SD-WACCM-X (Figures 6c and 6d) and HIAMCM (Figures 6e and 6f) simulations similarly suggest a nearly constant phase with altitude above 200 km. In their simulations, Miyoshi et al. (2009) similarly reported a nearly constant phase line with altitude above 250 km, descending with local time below. Below 200 km, both simulations show a descent of the phase line with local time, possibly indicating upward wave propagation. The variation with altitude for the NH summer case for MIGHTI observations and SD-WACCM-X simulations are presented in Figure 7.

4. Discussion

While STWs are believed to arise from traveling atmospheric pressure and temperature gradients, precisely where they originate in the atmosphere remains uncertain. Bespalova et al. (2016) suggested that neutral density perturbations observed following the ST might result from gravity waves generated in situ in the thermosphere by solar extreme ultra violet (EUV) heating gradients. In contrast, based on modeling results with and without lower atmospheric effects, Miyoshi et al. (2009) suggested that STWs may propagate up from the lower atmosphere, possibly in line with Chimonas and Hines (1970)'s initial proposal of STW generation initiated by heating due to UV absorption by middle atmospheric ozone.

Our analysis reveals a significant STW signature in solstice neutral wind observations. Both SD-WACCM-X and HIAMCM simulations capture the STW scale size and inclination relative to the ST, although the simulated STWs exceed the observed STW amplitudes. In contrast, TIEGCM simulations lack the STW signature, although

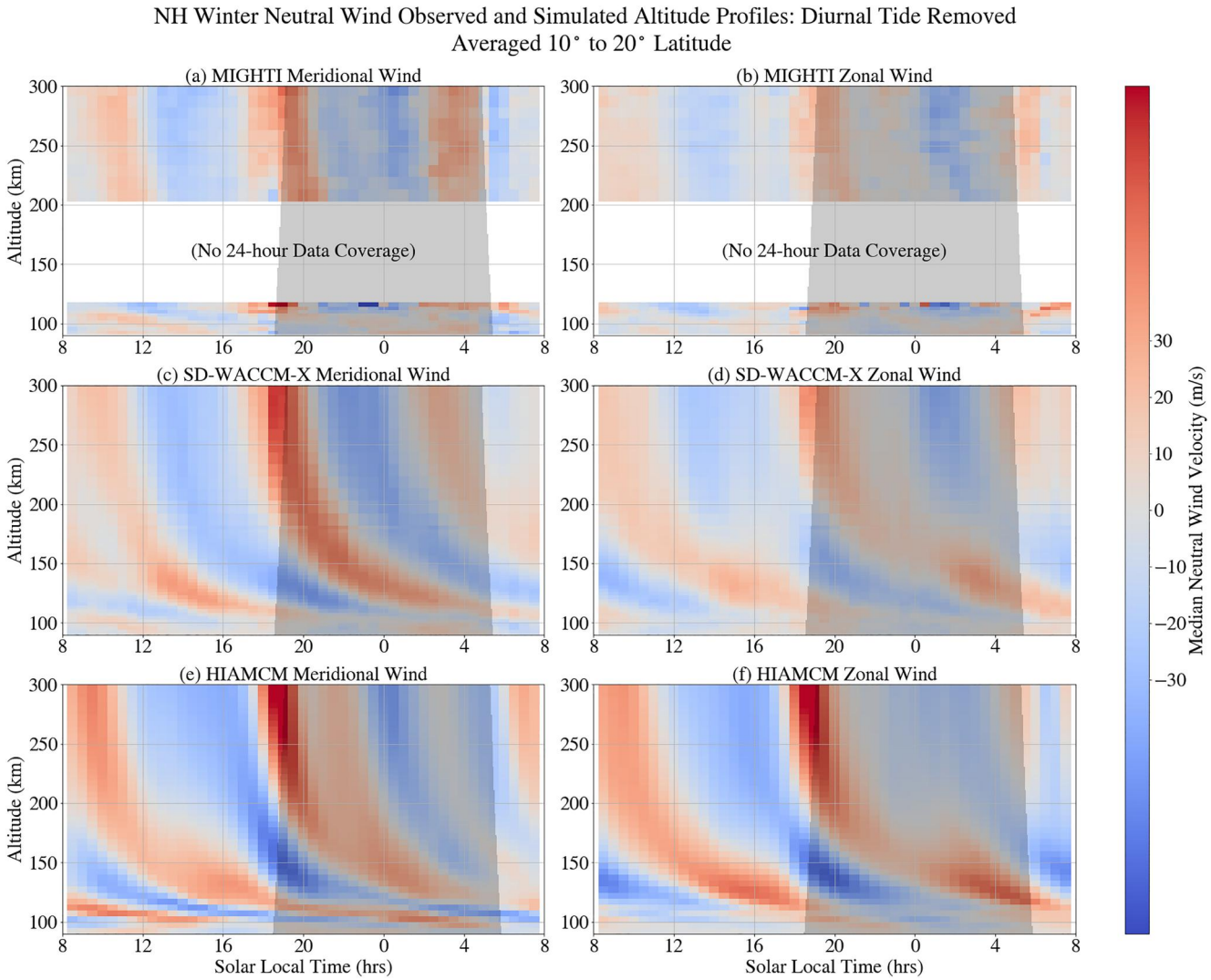

Figure 6. NH winter meridional (left) and zonal (right) winds averaged between 10° and 20° latitude as a function of altitude and SLT for (top) MIGHTI data (winter 2019 and 2020), (middle) SD-WACCM-X simulations (winter 2019 and 2020), and (bottom) HIAMCM simulations (15 January 2022). Diurnal tides have been removed. The gray shading shows the portion of the altitude/SLT space that is in darkness. Northward and eastward winds are defined to be positive.

introducing HMEs at the lower boundary leads to the emergence of a weak (~25 m/s) signature in the meridional wind component.

Both SD-WACCM-X and HIAMCM simulate the atmosphere down to Earth's surface (Becker & Vadas, 2020; H.-L. Liu et al., 2018), whereas the TIEGCM cannot self-consistently resolve atmospheric processes below its 97 km lower boundary (Qian et al., 2014). Including ICON HMEs into the TIEGCM partially accounts for lower atmospheric effects by including data-informed diurnal and semidirunal tidal propagation up from the lower atmosphere (Maute et al., 2023), suggesting that global-scale waves from the lower atmosphere may play a role in STW generation. The presence of STW signatures in models with the lower atmosphere but their absence in those without suggests that the lower atmosphere plays an important role in STW generation. This aligns with Miyoshi et al. (2009), who found that excluding atmospheric dynamics below 80 km in their simulations resulted in the disappearance of STW signatures. Further, the weak STW signature in the TIEGCM simulations with ICON HMEs implies that diurnal and semidiurnal tides from the lower and middle atmosphere contribute to, but cannot fully explain, the STW. Although Miyoshi et al. (2009) found that upward propagating migrating tides contributed to STW formation, they suggested that STWs mainly arise from a superposition of these tides with zonal wavenumbers 4 to 6, while our results suggest that lower-order tides also play an important role.

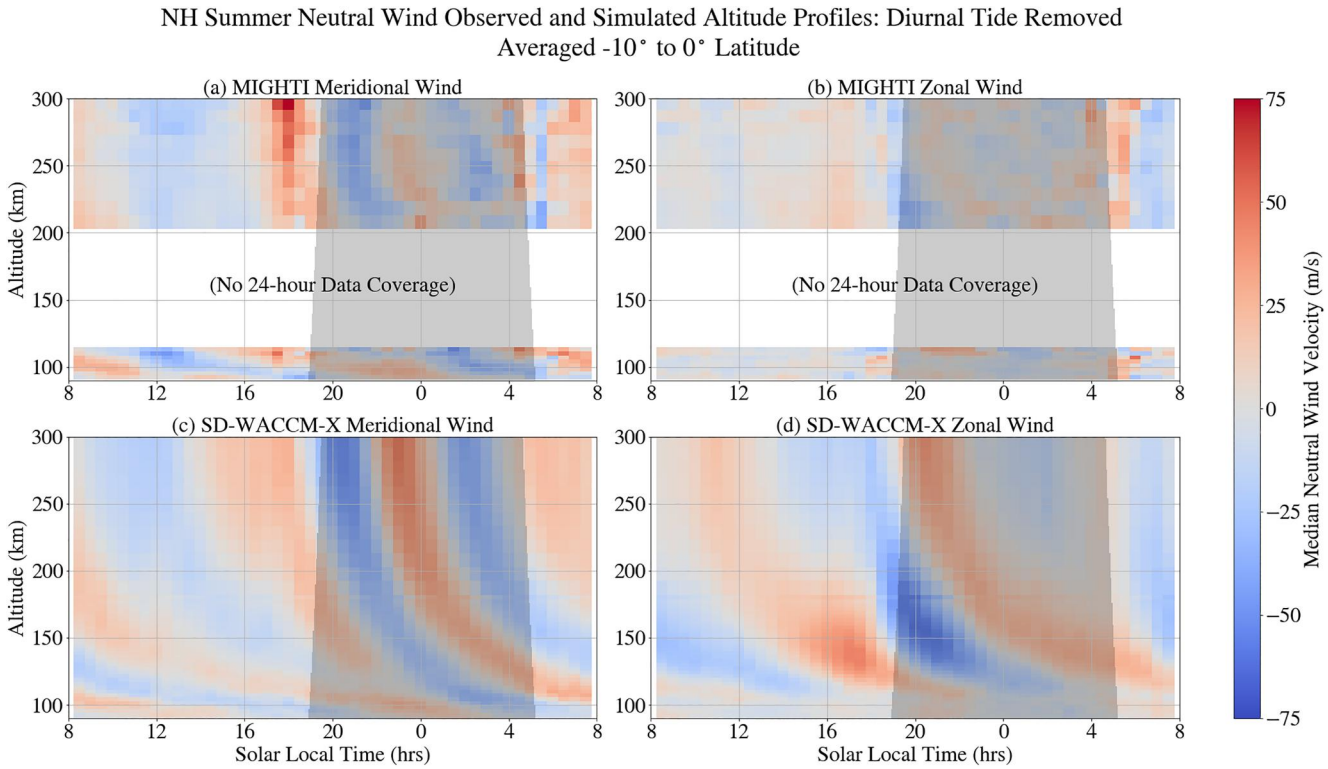

Figure 7. NH summer meridional (left) and zonal (right) winds averaged between −10° and 0° latitude as a function of altitude and SLT for (top) MIGHTI data (winter 2019 and 2020), (bottom) SD-WACCM-X simulations (winter 2019 and 2020). Diurnal tides have been removed. The gray shading shows the portion of the altitude/SLT space that is in darkness. Northward and eastward winds are defined to be positive.

Differences in how the models account for gravity wave effects may also affect their ability to reproduce STWs. STWs could be generated in part by large-scale gravity waves which either propagate directly from the lower/middle atmosphere to the thermosphere, or which are indirectly generated in the thermosphere through the dissipation of upward-propagating gravity waves (Heale et al., 2014; Lund & Fritts, 2012; Vadas, 2007). This latter "indirect" mechanism would arise because gravity wave dissipation by molecular viscosity depends critically on the background temperature, resulting in larger amplitude force/heating at lower altitudes on the nightside of the ST (Vadas, 2007). The resulting "jump" in the force/heating across the ST from gravity wave dissipation could then generate large-scale secondary gravity waves (Vadas, 2013).

Large-scale gravity waves arising from the ST passage would be captured by SD-WACCM-X and the HIAMCM, which resolve gravity waves from below, but not by the TIEGCM. Although direct EUV heating can also generate gravity waves (Chimonas & Hines, 1970; Vadas, 2013), the absence of STWs in the TIEGCM simulations suggests this mechanism is less significant. Notably, the amplitudes of stratospheric gravity waves have been found to be larger during solstice than equinox (Figure 6 of Cullens et al., 2022; Hoffmann et al., 2013), consistent with our finding of larger STW amplitudes during solstices, further supporting their potential connection to gravity waves. Furthermore, previous modeling and observations indicate that large (hundreds of kilometers) vertical wavelengths, like those we have observed for STWs, are consistent with a spectrum of gravity waves (Nicolls et al., 2014; Vadas, 2007; Vadas & Nicolls, 2009).

Future modeling studies will investigate these mechanisms, as well as possible non-linear tidal interactions, as the source of the STWs. Furthermore, the reason for the evening STW's inclination with respect to the ST remains an open question which future modeling should address.

Although we reported significant evening STWs, we do not observe any comparable signature near the morning ST. Both Forbes et al. (2008) and H. Liu et al. (2009) also noted this asymmetry, finding morning STWs to be less well-defined than their evening counterparts. H. Liu et al. (2009) postulated that larger neutral temperature gradients near the evening ST, as suggested by modeled neutral temperatures at 400 km, may make wave

generation more efficient in the evening. Some authors suggested the opposite, claiming that the morning heating process is more efficient than evening cooling, resulting in a sharper sunrise gradient which produces smaller scale STWs (Somsikov & Ganguly, 1995).

Indeed, both Chou et al. (2022) and Vadas et al. (2023) report a smaller scale, weaker amplitude morning STW in their simulation results. Ionospheric studies have also shown evidence of morning STWs (Afraimovich, 2008; Ding et al., 2014; Galushko et al., 1998; Song et al., 2013). For example, Zhang et al. (2021) measured post-sunrise electron density perturbations using the Millstone Hill Incoherent Scatter Radar (ISR), identifying traveling ionospheric disturbances (TIDs) with zonal wavelengths of ∼445 km. If similarly sized thermospheric disturbances accompany these TIDs, it is unlikely that MIGHTI would be able to resolve them due to its horizontal resolution.

The thermospheric evening STW may play a currently under-recognized role in driving ionospheric dynamics. The large-amplitude winds reported in this study could influence ionospheric circulation through ion drag or dynamo effects. The meridional STW winds can push plasma along magnetic field lines, contributing to the summer to winter hemisphere redistribution of plasma (Heelis et al., 2022) and affecting the plasma density altitude distribution. Additionally, the F-Region zonal STW winds, when blowing across the westward conductivity gradient caused by changing solar input, may influence the upward plasma drifts of the prereversal enhancement (PRE) (Eccles et al., 2015; H.-L. Liu, 2020; Richmond et al., 2015). Variability in STWs may thus affect the PRE, which, in turn, is closely linked to equatorial plasma bubble (EPB) variability (Fejer et al., 1999).

5. Conclusion

Leveraging ∼1.5 years of MIGHTI data, this study reported the first remotely sensed observations of evening STWs, revealing them as one of the most prominent recurring features in the neutral winds above 200 km during solstices. The STW meridional wind component, reported for the first time, has a similar (and sometimes larger) magnitude compared to the zonal component, indicating that STW winds blow predominantly northeastward during NH winter and southeastward during NH summer. Furthermore, we provided the first observational altitude profile of a STW, revealing vertical wavelengths longer than several hundred kilometers above 200 km. Model comparisons suggested that STW generation is strongly influenced by the lower atmosphere and may result from large-scale gravity waves or their interactions with atmospheric tides.

Given their substantial and persistent presence, STWs hold intrinsic scientific significance, potentially serving as key drivers of thermospheric and ionospheric processes. Future research endeavors, including modeling and observations, are crucial for unraveling the origins and daily variability of these waves, fostering a deeper understanding of their impact on Earth's upper atmosphere.

Data Availability Statement

This analysis used ICON/MIGHTI neutral wind data, Level 2.2, Version 5, which is available from https://icon.ssl.berkeley.edu/Data and https://cdaweb.gsfc.nasa.gov/pub/data/icon/ (Harding et al., 2023a, 2023b). The WACCM-X simulations used in this work are available from https://doi.org/10.5065/rjgt-g951 (Maute & HAO WACCM team, 2022). The TIEGCM-ICON simulations Level 4 V01 are available at https://cdaweb.gsfc.nasa.gov/pub/data/icon/l4/ (Maute & ICON Team, 2022). The HIAMCM simulation is available at https://www.cora.nwra.com/vadas/Vadas-etal-JGR-2023-TongaICON-files/ (Becker & Vadas, 2022).

Acknowledgments
ICON is supported by NASA's Explorers Program through contracts NNG12FA45C and NNG12FA42I. LCG was supported by NASA grant 80NSSC21K1386. SLV and EB were supported by NSF Grant AGS-1832988 and NASA Grant 80NSSC22K0174. AM is supported by NASA award 80NSSC23K1123.

References

Afraimovich, E. (2008). First GPS-TEC evidence for the wave structure excited by the solar terminator. *Earth Planets and Space*, *60*(8), 895–900. https://doi.org/10.1186/bf03352843

Becker, E., Goncharenko, L., Harvey, V. L., & Vadas, S. L. (2022). Multi-step vertical coupling during the January 2017 sudden stratospheric warming. *Journal of Geophysical Research: Space Physics*, *127*(12), e2022JA030866. https://doi.org/10.1029/2022ja030866

Becker, E., & Vadas, S. L. (2020). Explicit global simulation of gravity waves in the thermosphere. *Journal of Geophysical Research: Space Physics*, *125*(10), e2020JA028034. https://doi.org/10.1029/2020ja028034

Becker, E., & Vadas, S. L. (2022). HIAMCM background run January 15, 2022 [Dataset]. NWRA. Retrieved from https://www.cora.nwra.com/vadas/Vadas-etal-JGR-2023-TongaICON-files/HIAMCM_data_0-400km_5min/nomeso-0-400km_15JAN2022_00-23p9UT.hzti_zlev.dat

Becker, E., Vadas, S. L., Bossert, K., Harvey, V. L., Zülicke, C., & Hoffmann, L. (2022). A high-resolution whole-atmosphere model with resolved gravity waves and specified large-scale dynamics in the troposphere and stratosphere. *Journal of Geophysical Research: Atmospheres*, *127*(2), e2021JD035018. https://doi.org/10.1029/2021jd035018

Beer, T. (1973). Supersonic generation of atmospheric waves. *Nature*, *242*(5392), 34. https://doi.org/10.1038/242034a0

Beer, T. (1978). On atmospheric wave generation by the terminator. *Planetary and Space Science*, *26*(2), 185–188. https://doi.org/10.1016/0032-0633(78)90017-x

Bespalova, A., Fedorenko, A., Cheremnykh, O., & Zhuk, I. (2016). Satellite observations of wave disturbances caused by moving solar terminator. *Journal of Atmospheric and Solar-Terrestrial Physics*, *140*, 79–85. https://doi.org/10.1016/j.jastp.2016.02.012

Chimonas, G., & Hines, C. O. (1970). Atmospheric gravity waves induced by a solar eclipse. *Journal of Geophysical Research*, *75*(4), 875. https://doi.org/10.1029/JA075i004p00875

Chou, M.-Y., Yue, J., Sassi, F., McDonald, S., Tate, J., Pedatella, N., et al. (2022). Modeling the day-to-day variability of midnight equatorial plasma bubbles with SAMI3/SD-WACCM-X. *Journal of Geophysical Research: Space Physics*, *128*(5), e2023JA031585. https://doi.org/10.1029/2023ja031585

Colonna, R., & Tramutoli, V. (2021). A new model of solar illumination of Earth's atmosphere during night-time. *Earth*, *2*(2), 191–207. https://doi.org/10.3390/earth2020012

Cot, C., & Teitelbaum, H. (1980). Generation of gravity waves by inhomogeneous heating of the atmosphere. *Journal of Atmospheric and Terrestrial Physics*, *42*(9–10), 877–883. https://doi.org/10.1016/0021-9169(80)90092-6

Cullens, C. Y., England, S. L., Immel, T. J., Maute, A., Harding, B. J., Triplett, C. C., et al. (2022). Seasonal variations of medium-scale waves observed by ICON-MIGHTI. *Geophysical Research Letters*, *49*(17), e2022GL099383. https://doi.org/10.1029/2022gl099383

Cullens, C. Y., Immel, T. J., Triplett, C. C., Wu, Y.-J., England, S. L., Forbes, J. M., & Liu, G. (2020). Sensitivity study for ICON tidal analysis. *Progress in Earth and Planetary Science*, *7*, 1–13. https://doi.org/10.1186/s40645-020-00330-6

Ding, F., Wan, W., Li, Q., Zhang, R., Song, Q., Ning, B., et al. (2014). Comparative climatological study of large-scale traveling ionospheric disturbances over North America and China in 2011–2012. *Journal of Geophysical Research: Space Physics*, *119*(1), 519–529. https://doi.org/10.1002/2013ja019523

Drob, D., Emmert, J., Crowley, G., Picone, J., Shepherd, G., Skinner, W., et al. (2008). An empirical model of the Earth's horizontal wind fields: HWM07. *Journal of Geophysical Research*, *113*(A12), A12304. https://doi.org/10.1029/2008ja013668

Eccles, J., St. Maurice, J., & Schunk, R. W. (2015). Mechanisms underlying the prereversal enhancement of the vertical plasma drift in the low-latitude ionosphere. *Journal of Geophysical Research: Space Physics*, *120*(6), 4950–4970. https://doi.org/10.1002/2014ja020664

England, S. L., Englert, C. R., Harding, B. J., Triplett, C. C., Marr, K., Harlander, J. M., et al. (2022). Vertical shears of horizontal winds in the lower thermosphere observed by ICON. *Geophysical Research Letters*, *49*(11), e2022GL098337. https://doi.org/10.1029/2022gl098337

Englert, C. R., Harlander, J. M., Brown, C. M., Marr, K. D., Miller, I. J., Stump, J. E., et al. (2017). Michelson interferometer for global high-resolution thermospheric imaging (MIGHTI): Instrument design and calibration. *Space Science Reviews*, *212*(1–2), 553–584. https://doi.org/10.1007/s11214-017-0358-4

Englert, C. R., Harlander, J. M., Marr, K. D., Harding, B. J., Makela, J. J., Fae, T., et al. (2023). Michelson interferometer for global high-resolution thermospheric imaging (MIGHTI) on-orbit wind observations: Data analysis and instrument performance. *Space Science Reviews*, *219*(3), 27. https://doi.org/10.1007/s11214-023-00971-1

Fejer, B. G., Scherliess, L., & De Paula, E. (1999). Effects of the vertical plasma drift velocity on the generation and evolution of equatorial spread F. *Journal of Geophysical Research*, *104*(A9), 19859–19869. https://doi.org/10.1029/1999ja900271

Forbes, J., Bruinsma, S. L., Miyoshi, Y., & Fujiwara, H. (2008). A solar terminator wave in thermosphere neutral densities measured by the CHAMP satellite. *Geophysical Research Letters*, *35*(14), L14802. https://doi.org/10.1029/2008gl034075

Forbes, J., Zhang, X., Hagan, M. E., England, S. L., Liu, G., & Gasperini, F. (2017). On the specification of upward-propagating tides for ICON science investigations. *Space Science Reviews*, *212*(1–2), 697–713. https://doi.org/10.1007/s11214-017-0401-5

Galushko, V., Paznukhov, V., Yampolski, Y., & Foster, J. (1998). Incoherent scatter radar observations of AGW/TID events generated by the moving solar terminator. In *Annales geophysicae* (Vol. 16, pp. 821–827).

Garcia, R. R., Smith, A. K., Kinnison, D. E., de la Cámara, Á., & Murphy, D. J. (2017). Modification of the gravity wave parameterization in the whole atmosphere community climate model: Motivation and results. *Journal of the Atmospheric Sciences*, *74*(1), 275–291. https://doi.org/10.1175/jas-d-16-0104.1

Harding, B. J., Chau, J. L., He, M., Englert, C. R., Harlander, J. M., Marr, K. D., et al. (2021). Validation of ICON-MIGHTI thermospheric wind observations: 2. Green-line comparisons to specular meteor radars. *Journal of Geophysical Research: Space Physics*, *126*(3), e2020JA028947. https://doi.org/10.1029/2020ja028947

Harding, B. J., Englert, C. R., Harlander, J. M., Marr, K. D., Makela, J. M., Brown, C. M., et al. (2023a). ICON Michelson interferometer for global high-resolution thermospheric imaging wind vectors red (Version 05) [Dataset]. NASA Space Physics Data Facility. https://doi.org/10.48322/pyfw-zv85

Harding, B. J., Englert, C. R., Harlander, J. M., Marr, K. D., Makela, J. M., Brown, C. M., et al. (2023b). ICON Michelson interferometer for global high-resolution thermospheric imaging wind vectors green (Version 05) [Dataset]. NASA Space Physics Data Facility. https://doi.org/10.48322/vtce-7y29

Harding, B. J., Makela, J. J., Englert, C. R., Marr, K. D., Harlander, J. M., England, S. L., & Immel, T. J. (2017). The MIGHTI wind retrieval algorithm: Description and verification. *Space Science Reviews*, *212*(1–2), 585–600. https://doi.org/10.1007/s11214-017-0359-3

Harlander, J. M., Englert, C. R., Brown, C. M., Marr, K. D., Miller, I. J., Zastera, V., et al. (2017). Michelson interferometer for global high-resolution thermospheric imaging (MIGHTI): Monolithic interferometer design and test. *Space Science Reviews*, *212*(1–2), 601–613. https://doi.org/10.1007/s11214-017-0374-4

Heale, C., Snively, J., Hickey, M., & Ali, C. (2014). Thermospheric dissipation of upward propagating gravity wave packets. *Journal of Geophysical Research: Space Physics*, *119*(5), 3857–3872. https://doi.org/10.1002/2013ja019387

Heelis, R. A., Chen, Y.-J., Depew, M., Harding, B. J., Immel, T. J., Wu, Y.-J., et al. (2022). Topside plasma flows in the equatorial ionosphere and their relationships to F-region winds near 250 km. *Journal of Geophysical Research: Space Physics*, *127*(5), e2022JA030415. https://doi.org/10.1029/2022ja030415

Hoffmann, L., Xue, X., & Alexander, M. (2013). A global view of stratospheric gravity wave hotspots located with Atmospheric Infrared Sounder observations. *Journal of Geophysical Research: Atmospheres*, *118*(2), 416–434. https://doi.org/10.1029/2012jd018658

Immel, T. J., England, S., Mende, S., Heelis, R., Englert, C., Edelstein, J., et al. (2018). The ionospheric connection explorer mission: Mission goals and design. *Space Science Reviews*, *214*, 1–36. https://doi.org/10.1007/s11214-017-0449-2

Immel, T. J., England, S. L., Harding, B. J., Wu, Y.-J., Maute, A., Cullens, C., et al. (2023). The ionospheric connection explorer-prime mission review. *Space Science Reviews*, *219*(5), 41. https://doi.org/10.1007/s11214-023-00975-x

Lindzen, R. S. (1981). Turbulence and stress owing to gravity wave and tidal breakdown. *Journal of Geophysical Research*, *68*(C10), 9707–9714. https://doi.org/10.1029/jc086ic10p09707

Liu, H., Lühr, H., & Watanabe, S. (2009). A solar terminator wave in thermospheric wind and density simultaneously observed by CHAMP. *Geophysical Research Letters*, *36*(10), L10109. https://doi.org/10.1029/2009gl038165

Liu, H.-L. (2020). Day-to-day variability of prereversal enhancement in the vertical ion drift in response to large-scale forcing from the lower atmosphere. *Space Weather*, *18*(4), e2019SW002334. https://doi.org/10.1029/2019sw002334

Liu, H.-L., Bardeen, C. G., Foster, B. T., Lauritzen, P., Liu, J., Lu, G., et al. (2018). Development and validation of the whole atmosphere community climate model with thermosphere and ionosphere extension (WACCM-X 2.0). *Journal of Advances in Modeling Earth Systems*, *10*(2), 381–402. https://doi.org/10.1002/2017ms001232

Lund, T. S., & Fritts, D. C. (2012). Numerical simulation of gravity wave breaking in the lower thermosphere. *Journal of Geophysical Research*, *117*(D21), D21105. https://doi.org/10.1029/2012jd017536

Marsh, D. R., Mills, M. J., Kinnison, D. E., Lamarque, J.-F., Calvo, N., & Polvani, L. M. (2013). Climate change from 1850 to 2005 simulated in CESM1 (WACCM). *Journal of Climate*, *26*(19), 7372–7391. https://doi.org/10.1175/jcli-d-12-00558.1

Maute, A. (2017). Thermosphere-ionosphere-electrodynamics general circulation model for the ionospheric connection explorer: TIEGCM-ICON. *Space Science Reviews*, *212*(1–2), 523–551. https://doi.org/10.1007/s11214-017-0330-3

Maute, A., & HAO WACCM team. (2022). WACCMX-SD V2 [Dataset]. UCAR/NCAR - CISL - CDP. https://doi.org/10.5065/RJGT-G951

Maute, A., & ICON Team. (2022). TIEGCM-ICON [Dataset]. NASA. Retrieved from https://cdaweb.gsfc.nasa.gov/pub/data/icon/l4/

Maute, A., Forbes, J. M., Cullens, C. Y., & Immel, T. J. (2023). Delineating the effect of upward propagating migrating solar tides with the TIEGCM-ICON. *Frontiers in Astronomy and Space Sciences*, *10*, 1147571. https://doi.org/10.3389/fspas.2023.1147571

McGinness, E. C., Immel, T. J., Harding, B. J., Wu, Y.-J., & Triplett, C. C. (2023). The effects of a small geomagnetic storm on earth's thermosphere and ionosphere: ICON observations of the 25 January 2021 disturbance. *Journal of Geophysical Research: Space Physics*, *128*(7), e2022JA031207. https://doi.org/10.1029/2022ja031207

Miyoshi, Y., Fujiwara, H., Forbes, J. M., & Bruinsma, S. L. (2009). Solar terminator wave and its relation to the atmospheric tide. *Journal of Geophysical Research*, *114*(A7), A07303. https://doi.org/10.1029/2009ja014110

Neale, R. B., Richter, J., Park, S., Lauritzen, P. H., Vavrus, S. J., Rasch, P. J., & Zhang, M. (2013). The mean climate of the Community Atmosphere Model (CAM4) in forced SST and fully coupled experiments. *Journal of Climate*, *26*(14), 5150–5168. https://doi.org/10.1175/jcli-d-12-00236.1

Nicolls, M. J., Vadas, S. L., Aponte, N., & Sulzer, M. P. (2014). Horizontal parameters of daytime thermospheric gravity waves and E region neutral winds over Puerto Rico. *Journal of Geophysical Research: Space Physics*, *119*(1), 575–600. https://doi.org/10.1002/2013ja018988

Picone, J., Hedin, A., Drob, D. P., & Aikin, A. (2002). NRLMSISE-00 empirical model of the atmosphere: Statistical comparisons and scientific issues. *Journal of Geophysical Research*, *107*(A12), SIA15-1–SIA15-16. https://doi.org/10.1029/2002ja009430

Qian, L., Burns, A. G., Emery, B. A., Foster, B., Lu, G., Maute, A., et al. (2014). The NCAR TIE-GCM: A community model of the coupled thermosphere/ionosphere system. *Modeling the ionosphere–thermosphere system*, 73–83.

Richmond, A. (1995). Ionospheric electrodynamics using magnetic apex coordinates. *Journal of Geomagnetism and Geoelectricity*, *47*(2), 191–212. https://doi.org/10.5636/jgg.47.191

Richmond, A., Fang, T.-W., & Maute, A. (2015). Electrodynamics of the equatorial evening ionosphere: 1. Importance of winds in different regions. *Journal of Geophysical Research: Space Physics*, *120*(3), 2118–2132. https://doi.org/10.1002/2014ja020934

Richter, J. H., Sassi, F., & Garcia, R. R. (2010). Toward a physically based gravity wave source parameterization in a general circulation model. *Journal of the Atmospheric Sciences*, *67*(1), 136–156. https://doi.org/10.1175/2009jas3112.1

Somsikov, V. (1987). A spherical model of wave generation in the atmosphere by the solar terminator. *Journal of Atmospheric and Terrestrial Physics*, *49*(5), 433–438. https://doi.org/10.1016/0021-9169(87)90037-7

Somsikov, V. (2011). Solar terminator and dynamic phenomena in the atmosphere: A review. *Geomagnetism and Aeronomy*, *51*(6), 707–719. https://doi.org/10.1134/s0016793211060168

Somsikov, V., & Ganguly, B. (1995). On the formation of atmospheric inhomogeneities in the solar terminator region. *Journal of Atmospheric and Terrestrial Physics*, *57*(12), 1513–1523. https://doi.org/10.1016/0021-9169(95)00014-s

Song, Q., Ding, F., Wan, W., Ning, B., Liu, L., Zhao, B., et al. (2013). Statistical study of large-scale traveling ionospheric disturbances generated by the solar terminator over China. *Journal of Geophysical Research: Space Physics*, *118*(7), 4583–4593. https://doi.org/10.1002/jgra.50423

Vadas, S. L. (2007). Horizontal and vertical propagation and dissipation of gravity waves in the thermosphere from lower atmospheric and thermospheric sources. *Journal of Geophysical Research*, *112*(A6), A06305. https://doi.org/10.1029/2006ja011845

Vadas, S. L. (2013). Compressible f-plane solutions to body forces, heatings, and coolings, and application to the primary and secondary gravity waves generated by a deep convective plume. *Journal of Geophysical Research: Space Physics*, *118*(5), 2377–2397. https://doi.org/10.1002/jgra.50163

Vadas, S. L., Becker, E., Figueiredo, C., Bossert, K., Harding, B. J., & Gasque, L. C. (2023). Primary and secondary gravity waves and large-scale wind changes generated by the Tonga volcanic eruption on 15 January 2022: Modeling and comparison with ICON-MIGHTI winds. *Journal of Geophysical Research: Space Physics*, *128*(2), e2022JA031138. https://doi.org/10.1029/2022ja031138

Vadas, S. L., & Nicolls, M. J. (2009). Temporal evolution of neutral, thermospheric winds and plasma response using PFISR measurements of gravity waves. *Journal of Atmospheric and Solar-Terrestrial Physics*, *71*(6–7), 744–770. https://doi.org/10.1016/j.jastp.2009.01.011

Wu, Y.-J. J., Harding, B. J., Triplett, C. C., Makela, J. J., Marr, K. D., Englert, C. R., et al. (2020). Errors from asymmetric emission rate in spaceborne, limb sounding Doppler interferometry: A correction algorithm with application to ICON/MIGHTI. *Earth and Space Science*, *7*(10), e2020EA001164. https://doi.org/10.1029/2020ea001164

Wu, Y.-J. J., Mende, S., Harding, B. J., Alken, P., Maute, A., & Immel, T. J. (2023). Cross-validation of the ionospheric vertical drift measurements based on ICON/IVM, Swarm, and the ground-based radar at the Jicamarca radio observatory. *Space Science Reviews*, *219*(6), 47. https://doi.org/10.1007/s11214-023-00993-9

Zhang, S.-R., Erickson, P. J., Gasque, L., Aa, E., Rideout, W., Vierinen, J., et al. (2021). Electrified postsunrise ionospheric perturbations at Millstone Hill. *Geophysical Research Letters*, *48*(18), e2021GL095151. https://doi.org/10.1029/2021gl095151